View Article Online
DOI: 10.1039/D3CP00935A

Journal Name

ARTICLE TYPE

Cite this: DOI: 00.0000/xxxxxxxxxx

How physical properties of bacterial porins match environmental conditions†

Stefan Milenkovic,[ab] Jiajun Wang,[c] Silvia Acosta-Gutierrez,[d] Mathias Winterhalter,[e] Matteo Ceccarelli,*[ab] and Igor V. Bodrenko *[ac‡]

Received Date
Accepted Date

DOI: 00.0000/xxxxxxxxxx

Transmembrane β-barrel proteins are key systems for transport phenomena in biology. Based on their broad substrate specificity, they represent good candidates for present and future technological applications, such as DNA/RNA and protein sequencing, sensing of biomedical analytes, and production of blue energy. For a better understanding of the process at molecular level, we applied parallel tempering simulations in the WTE ensemble to compare two β-barrel porins from *Escherichia coli*, OmpF and OmpC. Our analysis showed a different behavior of the two highly homologous porins, where subtle amino acid substitutions can modulate critical properties of mass transport. Interestingly, the differences can be mapped to the respective environmental conditions at which the two porins are expressed. Apart from reporting on the advantages of the enhanced sampling methods in assessing the molecular properties of nanopores, our comparative analysis provided new and key results to understand better biological function and technical applications. Eventually, we showed how results from molecular simulations align well with experimental single-channel measurements, thus demonstrating the mature evolution of numerical methodologies for predicting properties in this field crucial for future biomedical applications.

1 Introduction

Transmembrane β-barrel proteins are key systems for biological functionalities.[1] Generally expressed in a membrane separating two different compartments and filled with bulk-like water molecules,[2] they work as electrostatic sieves controlling the transport of molecules.[3] Through their primary, secondary and tertiary structure, they modulate the strength of the molecules flux, with the selective control on (i) their size and (ii) their chemical composition. Two major classes of membrane transport proteins exist, the active transporters, known as Ton-B dependent transporters,[4] and the passive channels. Here we focus on the latter class, considering the non-specific diffusion channel proteins, namely the porins.[5] These channels have become extremely significant for technological applications[6] and understanding how molecules diffuse through nanopores is a scientific challenge in many fields. Nanopores are being used as sensors in biomedical laboratories: DNA/RNA sequencing with nanopores is cheaper, sustainable and portable;[7,8] new investigations aim to extend nanopore technologies to protein sequencing,[9] sensing of other analytes,[10] and the production of blue energy.[11] Recently, it has been demonstrated how these proteins can be designed by computational tools,[12] and screened with a high-throughput assay,[13] thus opening the engineered protein nanopores for further applications. Further, biological pores have inspired the design of syntehtic nanopores.[14]

Another compelling pharmaceutical application on the mass transport through nanopores is represented by the diffusive permeation of small molecules through porins of Gram-negative bacteria.[15] Although, we know that currently the permeability is considered to be the key element for the resistance of Gram-negative bacterial species to antibiotics,[16,17] our knowledge about permeation is still at a qualitative level since a robust and direct method to measure permeation does not exist yet.[18,19] For this reason, we haven't yet identified clear chemical rules to rationalize the permeation of antibiotics, contrary to the central nervous system drugs for which the Lipinsky rule of five applies[20]. Nevertheless, in the lack of efficient experimental alternatives, various molecular dynamics techniques represent promising tools for investigating the mechanism of permeation and quantifying the permeabil-

[a] *IOM/CNR Sezione di Cagliari, Cittadella Universitaria, 09042 Monserrato, Italy*
[b] *Dipartimento di Fisica, University of Cagliari, Cittadella Universitaria, 09042 Monserrato, Italy*
[e] *Department of Life Sciences and Chemistry, Jacobs University Bremen, 28759 Bremen, Germany*
[d] *Institute for Bioengineering of Catalonia, 08028 Barcelona, Spain*
[e] *School of Science, Constructor University, 28759 Bremen, Germany.*
* Email: matteo.ceccarelli@dsf.unica.it; igor.bodrenko@cnr.it

† Electronic Supplementary Information (ESI) available: [details of any supplementary information available should be included here]. See DOI: 00.0000/00000000.

‡ Present address: École Normale Supérieure, Département de Chimie - Laboratoire PASTEUR, Paris, France.

View Article Online
DOI: 10.1039/D3CP00935A

ity via free energy calculations.[21,22]

In recent years, by combining mass spectrometry accumulation data,[23] single-channel electrophysiology experiments,[24] and accelerated molecular dynamics simulations,[25] it has been shown that porins represent the main path of entry of polar antibiotics/inhibitors into enterobacter species,[26] such as OmpF and OmpC from *Escherichia coli*. Further, we have several examples of amino acid substitutions in porins that can affect susceptibility for antibiotics penetration and efficacy, thus pointing to an atomistically precise mechanism.[27–30] Our past contribution identified such a precise mechanism consisting of different molecule-pore physical interactions, namely a steric term[31] and a few more electrostatic terms,[24] to guide the development of a scoring function to predict permeability.[32,33] These interactions are deduced from the common features of porins, the size constriction and the internal transversal electric field.[3,34] Since bacteria express porins with small-sized pores in order to keep their internal integrity,[35] we noted that the average size of transported molecules is generally larger than the average size of porins[31], thus creating the steric term. Within this scenario, the evaluation of average size properties is not sufficient to predict permeability, and the use of distribution functions is mandatory.[36] In the light of these observations, we have developed a model which approximates the diffusion of molecules through nanopores as a steric problem, where the flexibility of both the pore and molecules are key parameters.[31] Very recently, the same approach proved itself useful when it was applied to unravel the mechanism of protein diffusion through the nuclear pore complex system.[37]

Another aspect that makes the mass transport problem more challenging is that the overlap between the two size distributions, those referring to the pore and the molecule, occurs on the tails at extreme values,[31] when for spontaneous fluctuations the pore becomes large and at the same time the molecule shrinks. Special algorithms are necessary to correctly sample the tails of distributions by extending the sampling to rare events, especially for the pore system. Although all-atom molecular dynamics simulations represent a proper tool to investigate proteins keeping their molecular details,[38] the ergodicity of the sampling is guaranteed only in few cases,[39] with specific methods selected according to the process under investigation.[40,41] Further, modeling of membrane proteins requires the proper treatment of the protein-membrane interactions by embedding them in a phospholipid bilayer.[42] This extra layer makes the system larger than solvated proteins, thus becoming more challenging for simulations. Here we show that for porins embedded in an explicit membrane the use of an enhanced sampling technique, the parallel tempering in the well-tempered ensemble,[43] is mandatory for sampling correctly the internal size of porins.

General bacterial porins are characterized by a beta-barrel homo-trimeric structure with long loops on the extracellular side.[33] In particular, the loop L3 can fold inside each monomer creating the characteristic hourglass shape (see Fig.1). The presence of a flexible element inside the eyelet is a feature present in diverse porins, such as the mitochondrial voltage-dependent anionic channels in eukaryotic cells (VDAC),[44] or the specific porins of other Gram-negative species (CymA).[35,45,46] Considered for

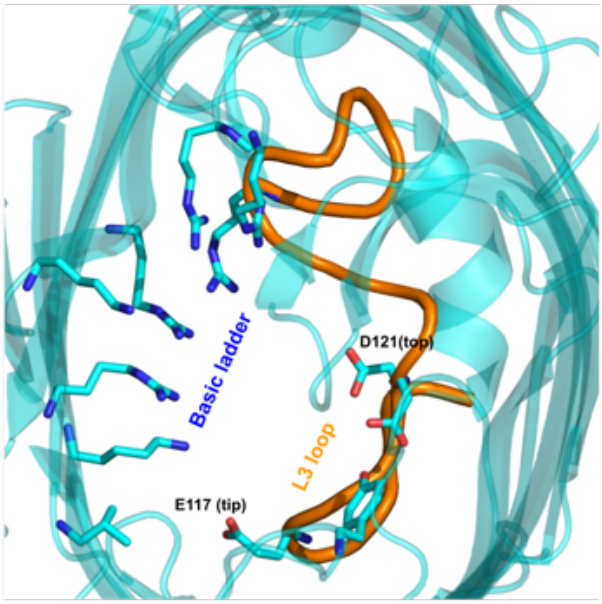

Fig. 1 Top view of the OmpF's constriction region: the basic ladder (composed of basic amino acid residues) is on the left, and the loop L3 with the three acidic residues (D113, E117 (tip), and D121 (top)) is on the right and colored orange.

many years as rigid proteins[47], contrarily to more flexible soluble proteins, the mobile element of β-barrel porins gained interest related to potential porin's functions recently: in VDAC it is reported to modulate the interaction with some enzymes;[48] in CymA it is able to modulate the transport, and as such it is considered as crucial for technological applications.[49] In OmpF it was suggested that the mobile element acts as a trigger for balancing the two states of the pore, respectively open and closed[50], arguing that the mobile element dynamics might be the origin of the resistance of bacteria to antibiotics, assuming that this can be a general mechanism for this family of porins with high degree of homology.

Here, we show that OmpC and OmpF owe their different functional environments (where each of them is dominantly expressed), to a few key differences in their primary structures. Upon the identification of a few key amino acids, we have confirmed their significance by simulating the corresponding OmpF mutant. The two aforementioned model porins[33] were compared by simulating them with the parallel tempering (PT) technique in the well-tempered ensemble[43]. In this way, we ensure enhanced sampling by simulating simultaneously at different temperatures ranging from 297 K to 345 K, with the latter close to the maximum stability temperature of porins[51]. We note that PT simulations have already shown a remarkable advantage for efficient sampling of loop conformations[52] and in our study, the PT technique extends beyond the limit of standard MD simulations and accurately predicts conformational dynamics of our nanopores.

In Fig.2 we reported the distributions of the minimum radius from (i) prePT MD (performed before PT), (ii) PT , and (iii) postPT MD simulations (performed after PT). We note that all distributions have the same tail for large values of the radius, and they peak approximately at the same value r_{min}=2.8-2.9 Å.

View Article Online
DOI: 10.1039/D3CP00935A

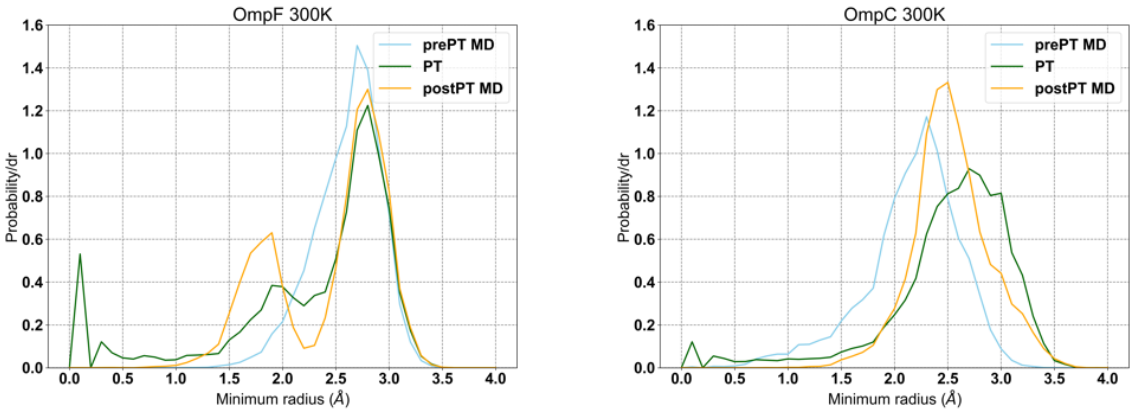

Fig. 2 Distribution of minimum radius for OmpF (left) and OmpC (right) simulations at 300K with focus on comparing parallel tempering replica at 300K (PT-green) with standard simulations performed before (prePT MD-skyblue) and after PT (postPT MD-orange).

However, striking differences are present at the lower end of the minimum radii distributions. The prePT MD distribution (sky-blue) is the most symmetric and decays to zero smoothly. On the other hand, the PT distribution (green) shows a not-negligible peak close to r_{min}=0 and a third peak at around r_{min}=1.9 Å. The peak at r_{min}=0 means the complete closure of the pore, indicated here as "gating peak". The prePT MD and PT distributions are remarkably different. When the effect of switching among replicas is turned off in post PT MD, we see that the distribution loses the gating peak and increases the intermediate peak at r_{min}=1.9 Å, but still shows more similarities to PT than prePT MD distribution. The presence of several conformational states in OmpF is in line with very recent results obtained by employing another computational approach and another force field, thus reinforcing the view of a flexible pore.[50]

2 Results and Discussion

2.1 Enhanced sampling

We simulated at the all-atom level the OmpF porin embedded in a POPC bilayer and solvated with water at 200 mM KCl concentration, close to expected physiological conditions. For each sampled conformation extracted from the 1 μs trajectories at 300K, we calculated two observables characterizing the eyelet region: (i) the minimum radius of the pore; (ii) the average internal radius and fluctuations along pore's axis.

The same analysis performed on OmpC shows a different outcome. The prePT MD distribution has the major peak at a smaller value than OmpF, r_{min}=2.2 Å, as in X-ray structures (see Tab.1), and a longer tail at low values of the radius. The effect of extended sampling on OmpC properties (PT) is twofold: (i) it shifts the major peak towards higher values, r_{min}=2.8 Å, and (ii) it favors the appearance of the gating peak, practically negligible in prePT MD. For OmpC the postPT MD distribution is more similar to PT than to prePT MD one, according to the shift of the major peak; on the other hand, the postPT MD distribution is different at the lower end, showing neither the long tail of the prePT MD distribution nor the presence of the gating peak as in PT distribution.

2.2 OmpF's vs OmpC's temperature sensitivity

The main difference in OmpF vs OmpC behavior is reflected in their temperature sensitivity. We calculated the distribution of pore radius on the 1 μs trajectory, together with its cumulative distribution, $P(r < r_0)$, to catch overall differences. Namely, we see in Fig. 3 that OmpC's and OmpF's responses to the temperature increase are astonishingly different. OmpC's pore dynamics remain the same, and we see that both, regular (solid lines) and cumulative (dashed lines) distributions remain unaltered when we move from 300 K (blue) to 345 K (magenta) PT replica. On contrary, OmpF's response is quite vivid. We note that the gating peak increases with the temperature increase whereas the intermediate peak appears to be "spread" between the major peak and the gating peak. In other words, the temperature increase creates two-state pore dynamics with an increased chance for gating.

2.3 L3 as gating element

In order to further characterize the differences between OmpF's and OmpC's dynamics relative to MD/PT approaches, we have focused on the dynamics of the internal L3 loop. Independently from what was published very recently,[50] we analyzed the gating of the two pores focusing on the movement of the mobile loop L3 with respect to the basic ladder, just in front of it (see Fig.1). We started by simply overlapping the conformations sampled along the PT trajectories, which suggests that L3 loop samples different conformations with an overall similar flexibility as seen in Fig.4.

To grasp and quantify these differences we have performed the principal component analysis (PCA). Here we show the largest principal component in both proteins, Fig. S**??** panel A and B, which appears to involve the L3 loop. Furthermore, we notice that OmpC and OmpF essentially react differently to the parallel tempering setup, with OmpC keeping its original dynamics obtained with standard MD (Fig. S**??**, panel C), and OmpF showing more flexibility in the L3 region (Fig. S**??**, panel D). The key difference emerges in the lower portion of the L3 loop, i.e. the portion responsible for the gating of the channel whereas the difference in OmpF's upper portion of the L3 finds its origin in the

View Article Online
DOI: 10.1039/D3CP00935A

Table 1 Various size parameters of OmpF/OmpC porins, extracted either from X-ray structures or averaged from molecular dynamics trajectories. For X-ray we reported the size calculated from two high-resolution structures, 2OMF and 2ZFG or 2J1N and 7JZ3, respectively for OmpF and OmpC

	X-ray/Å	<PrePT> /Å	<PT-300K>/Å	<PostPT>/Å
OmpF	2.78/2.78	2.56 ± 0.3 MAX-prob=2.7	2.25 ± 0.8 MAX-prob=2.8	2.40 ± 0.5 MAX-prob=2.8
OmpC	2.17/2.13	2.11 ± 0.4 MAX-prob=2.3	2.47 ± 0.6 MAX-prob=2.7	2.48 ± 0.4 MAX-prob=2.5

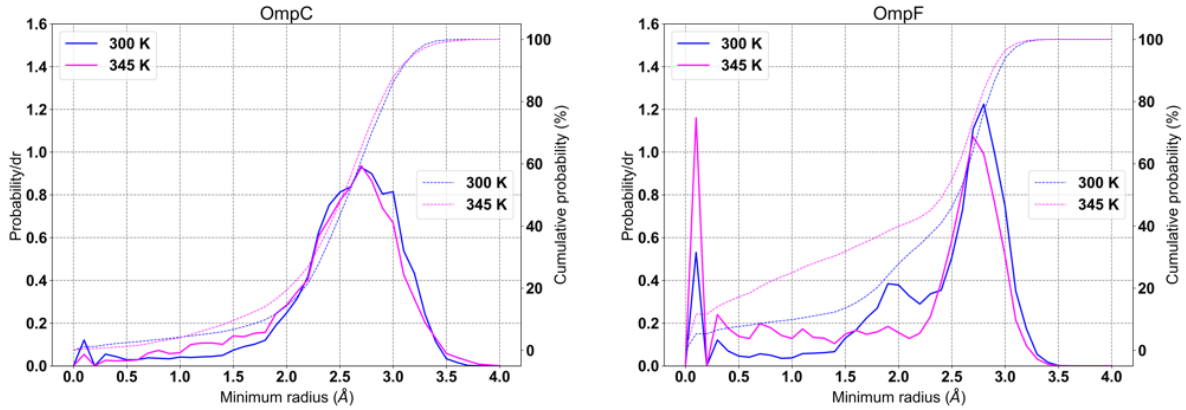

Fig. 3 Distributions of the pore minimum radius in OmpC (left) and OmpF (right) extracted from PT replicas at 300 K (blue) and 345 K (magenta). The dotted lines represent cumulative distributions of the radius, $P(r < r_0)$.

interaction of D121 with Y32, an amino acid native to OmpF (an inserted amino acid with respect to OmpC). Moreover, the entire change in dynamics can be understood as a change in hydrogen bonding interactions between the loop L3 and the rest of the protein, which is schematically summarized in Fig. S**??**. We note that in PT setup, D121 establishes connections with the lateral group of arginines upon the weakening of the D121-Y32 hydrogen bond. By inspecting the PT trajectories at 300 K, we identified specific inter-residue distances describing the two different gating movements: (i) the distance between the tip of the loop L3 (residue E117) and the central arginine (residue R82), (ii) the distance between the top of the loop L3 (residue D121) and the central arginine (residue R82). To note that in our analysis we selected R82 instead of R80 used in Ref.[50] to quantify the movement of the loop L3 since R80 is not conserved in OmpC. Furthermore, the visual inspection revealed that the tip of loop L3 (E117) is more stable in OmpC versus OmpF. On the other hand, in OmpF the top of the loop L3 (D121) is farther from the basic ladder than in OmpC; however, both pores show an important occurrence of gating with this movement. Interestingly, these differences can be assigned to subtle substitutions in residues around E117 and D121, as shown after the alignment of the two sequences (Fig. S**??**). At position 18, spatially close to E117, OmpC has an aspartic acid while OmpF has a valine. Thus the presence of D18, apart from changing the electric field[28], might decrease the movement of E117 toward the basic ladder due to electrostatic repulsion. The top of the L3 loop is stabilized in OmpF by a hydrogen bond between D121 and Y32, the latter being an insertion when we align the two sequences, thus not present in OmpC. The presence of this hydrogen bond might explain the longer D121-R82 distance in OmpF versus OmpC.

To check both hypotheses, we prepared the OmpF double mutant system (OmpF-2mut) where we substituted V18→D18 and Y32→G32. While for the former it was possible to use the corresponding residue in OmpC, for the latter we decided that the inserted residue at position 32 was substituted with the residue having the highest flexibility and smallest volume, glycine. Now, we have compared E117-R82 and D121-R82 distances (Fig. 5) for OmpC (orange), OmpF-2mut (yellow), and OmpF (green) simulations. We can clearly conclude that the mutated pore is much closer to OmpC than OmpF. The presence of the D18 makes the tip of L3 more rigid, with a low probability of flickering toward the basic ladder, and a larger maximum distance as in OmpC; the lack of the Y32 partner for hydrogen bond with D121 shifts the top of L3 toward the basic ladder, however without changing the probability for gating. The maximum peak is not exactly as in OmpC, probably because this movement is more complex than the flickering of the tip of L3, and it involves more residues, thus not accessible with our simple OmpF-2mut double mutant system.

The results obtained very recently by another group on OmpF gating are exactly in line with our results.[50] In this pore, the modulation of the constriction region is due to the loop L3, either the tip (E117) or the top (D121), or both. This confirms immediately that both force fields, amber (employed here) and charmm, are good for describing these porin systems. In addition, our analysis revealed subtle differences between OmpF and OmpC, by correlating them with proper amino acid substitutions. The movement of the top of loop L3 is not controlled by hydrogen bonds with Y32; the gating probability due to this movement does not change by eliminating that residue. However that hydrogen bond is im-

View Article Online
DOI: 10.1039/D3CP00935A

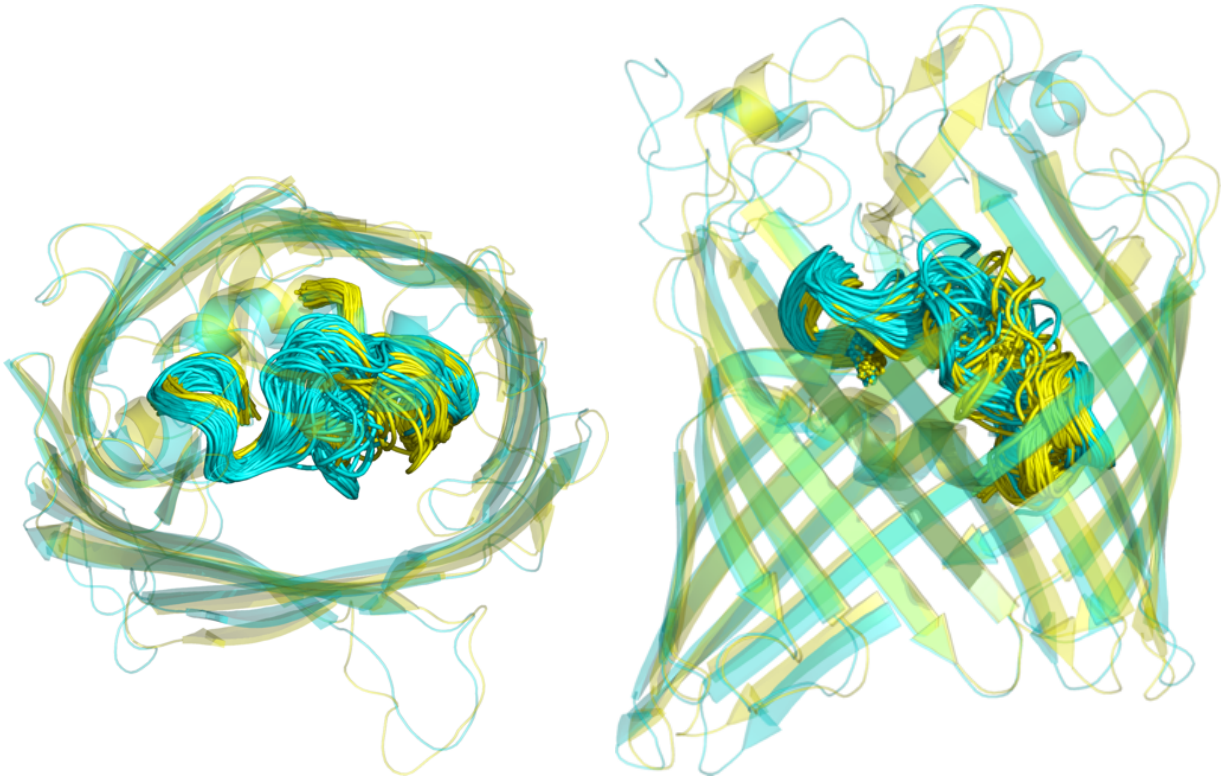

Fig. 4 (A) Top and (B) side view of the OmpF/OmpC structure alignment with OmpF in yellow and OmpC in cyan. The L3 loop is depicted as an overlap of many conformations extracted from the entire trajectory.

portant to keep the pore more open when in the open state and create a large space in the preorientation region to accomodate zwitterionic molecules (such as ampicillin and norfloxacin), thus increasing transport at low concentration. Instead, the closure of the pore due to the collapse of the loop L3 is controlled and perhaps initiated by the movement of the tip of the loop L3. Interestingly, the tip of loop L3 (Glu 117) is influenced by the charge of the neighbor residue at position 18. When at this position we have a neutral residue (a valine in OmpF), we see a shorter distance with the arginine ladder and possibility of gating; or a large distance and no gating when a charged residue occupies the position (an aspartic acid), as in the case of OmpC or the double mutant. The collapse of the top of the loop seems to come after the closure at the tip, thus hindering the movement of the latter there is less probability to gate.

2.4 Global effect of the double mutation

Because the evaluation of the flux of molecules along a pore of length L, over a free energy surface U(Z) and with diffusion constant D(Z), is determined by an integral over the entire pore,[32]

$$J = P\Delta C; \quad P = \left[\int_0^L \frac{exp(\beta U(z))}{D(Z)} dZ\right]^{-1}$$

we need to compare the size over the entire pore to establish real differences, taking into account also saturation effects.[53] We initiate by repeating the minimum pore radius analysis shown previously in Fig. 3 to obtain that the minimum pore radius distribution looks much more like the OmpC's distribution when subjected to temperature increase (Fig. 6).

Furthermore, we have compared the average pore radii along the pore axis (Fig.7, left) for OmpC, OmpF, and OmpF double mutant systems. The two porins have the same internal radius, within fluctuations, at the constriction region, with OmpF showing larger fluctuations than OmpC almost everywhere. The OmpF double mutant mostly average pore size profile largely resembles the one of the wild-type so we can conclude that mutations we have imposed do not alter pore conformation significantly. Nevertheless, the effect of the temperature increase on OmpF double mutant significantly differs from the effect that same temperature increase has on the wild-type. In Fig.7 (right), we see that the difference in fluctuations of the radius along the pore caused by the temperature increase. The highest value in the constriction region is recorded for OmpF, whereas the OmpF double mutant doesn't exhibit such a striking change and it has a profile closer to the OmpC. Once again, we can conclude that OmpF behaves very much differently than OmpC at higher temperatures and that the essence of this difference are the mutated residues.

It is worth mentioning that the largest structural difference between OmpF and OmpC is the region in the extracellular vestibule (10-15 Å from the center) present in OmpF which is characterized by larger size (Fig.2) and higher electric field, as we already pointed out.[34] We named it the pre-orientation region, because molecules are preoriented by the high electric field prior to enter the constriction region. Uniquelly to OmpF, this is also the region where ampicillin was co-crystallized[54] and we found a binding site for norfloxacin,[3] another dipolar molecule.

The existence of such a region, a sort of molecules' reservoir,

View Article Online
DOI: 10.1039/D3CP00935A

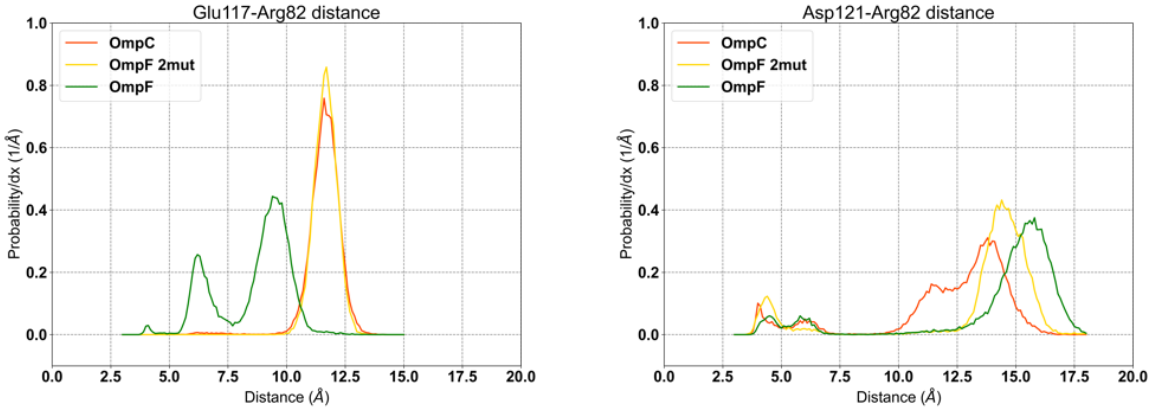

Fig. 5 Distribution of distances for OmpF (green), OmpC (orange), and the OmpF 2mut (yellow) as extracted from PT replica at 300K. (Left) Distance Glu117-Arg82 (tip of the loop L3 to the arginine cluster) and (right) distance Asp121-Arg82 (top of the loop L3 to the arginine cluster).

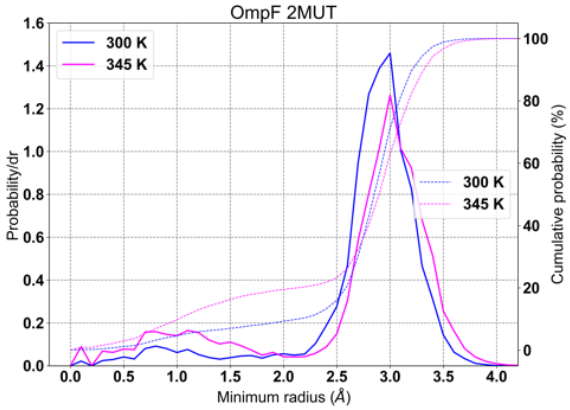

Fig. 6 Distributions of the pore minimum radius in OmpF-2mut extracted from PT replicas at 300 K (blue) and 345 K (magenta). The dotted lines represent cumulative distributions of respective variables.

helps OmpF to transport molecules efficiently even when present in solution at low concentration. The same effect was suggested by simulating the transport of glycerol through GlpF.[55] This is not the case for OmpC, where in the corresponding space, the pore is smaller and has a lower electric field. A numerical example was presented recently where the free energy and flux of a beta-lactamase inhibitor, tazobactam, through OmpF and OmpC[53] was compared. The lower free energy obtained for the extracellular eyelet region of OmpF corresponds exactly to the 10-15Å region where OmpF is larger than OmpC.

2.5 Experimental evidence.

In order to support our conclusion from modeling, we performed experiments on small-molecule transport through the pores by using single-channel electrophysiology. We reconstituted OmpF and OmpC porins in a lipid bilayer separating the two chambers (see Methods in SI). For OmpF, we measured the association rate k_{on}, for several antibiotics molecules as function of the (inverse) temperature. From Fig.8 we see that the association rates are not constant and differ according to the molecule employed. In particular, exactly at the same temperature of 298 K ($1/k_BT$=1.688 mol/Kcal) the slope of the curve changes, indicating a different regime, above and below that temperature, as shown by the straight lines. The slope of the curve indicates the enthalpic barrier to reach the internal affinity site, thus indicating a higher barrier above 298 K. According to our simulations and the recent results of Ref.[50], we can explain this change as an increased probability to gate for OmpF, causing a lower rate of entry for molecules. It is interesting that this change of regime is not depending on the molecule we are measuring, indicating thus a property of the pore not perturbed by the transported molecule. To gain more details, we focused our attention on a single molecule, ertapenem, comparing the association rate for OmpF versus OmpC, upon addition on both the cis and trans side. As reported in Fig.8 we can see that association of ertapenem to OmpC does not display the change of slope as function of temperature, exactly as in our simulations we do not see any change in the internal radius and gating between the two replicas at low temperature (300K) and high temperature (345K). Further, the change in association to OmpF as function of temperature happens only upon cis addition. This is not in contradiction with our model where the loop L3 closes the pore collapsing with the top part, or those residues facing the extracellular eyelet region, thus closing the association of ertapenem to the constriction region when added from the cis side only. Thus it seems that when we add ertapenem from the trans side there is no occlusion for reaching the affinity site, which we can imagine below the loop L3.

3 Conclusion

Interestingly the OmpF/OmpC subtle differences can be mapped to the different conditions at which the two porins are expressed. OmpF is expressed at normal conditions of temperature and osmolarity, while OmpC is expressed during infection, such as in the stomach for *E.coli*, when high temperature and osmolarity conditions are expected. Though the high homology of the two porins (85% similarity, 63% identity) our results showed subtle

View Article Online
DOI: 10.1039/D3CP00935A

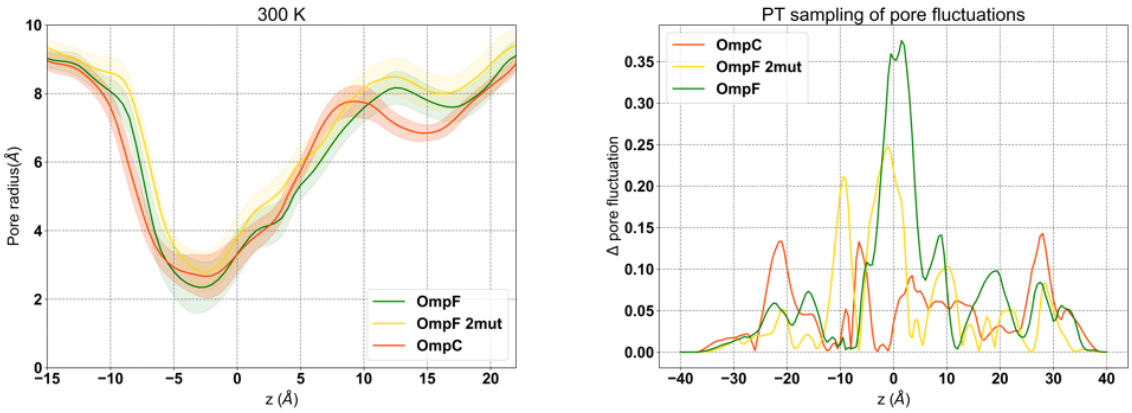

Fig. 7 (Left) The average pore radius of OmpF (green), OmpF 2mut (yellow), and OmpC (orange) with their respective fluctuations plotted as shade. (Right) The difference between fluctuations in PT replicas on 345 K and 300 K of each respective system. The coloring scheme corresponds to the left panel.

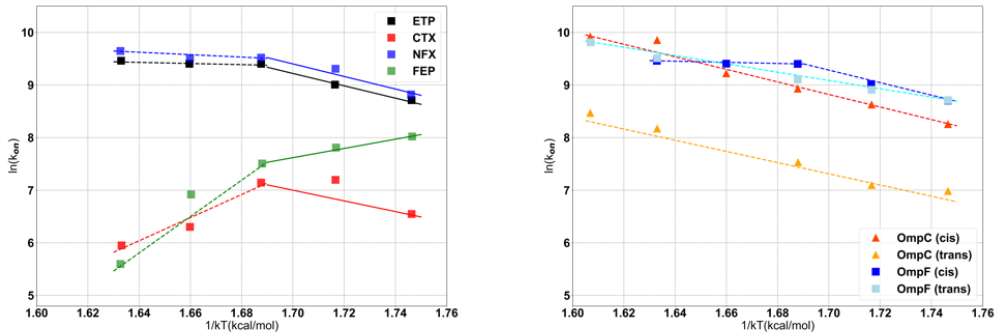

Fig. 8 Left: Association rate of different antibiotics in OmpF when added to the cis side, as function of inverse temperature. The lines are fitted on the first/last three points and represent eye-guide to underline the cusp (possible structural transition) at the same temperature. Right: association rate of ertapenem in OmpF and OmpC when added to either cis or trans side, as function of inverse temperature. The straight lines are fitted to all points but OmpF (cis).

differences, however key for their functioning in mass transport. OmpF fluctuates more than OmpC and gates more frequently, especially when increasing the temperature (Fig.3); OmpC on the other hand shows more stability at any temperature. An almost identical condition of stability of OmpC versus OmpF upon changing environmental conditions was put forward looking at the internal transversal electric field.[34] Though in OmpF the electric field is higher than in OmpC at very low ion concentration (35 versus 20 mV/Å), we saw a progressive decrease of the electric field upon increasing ionic concentrations to 200 mM and 400 mM. The same condition has no effect on the internal electric field of OmpC. Thus the two have the same electric field at high osmolarity conditions. OmpF would not be efficient in transport either with high-temperature conditions because of the high rate of gating, nor at high osmolarity (ions and solutes) because of potential saturation effects and a lower electric field; on the other hand, the more stable OmpC is more suitable to the expected conditions during infections.

We presented and tested a computational strategy to obtain key parameters of two relevant porins necessary for the prediction of the permeability of small molecules. We showed the importance of enhanced sampling simulations to evaluate the size and fluctuations of two relevant pores. Given the high acceptance rate reached (40%, see Table 3), there is still space to decrease the number of replicas, or increase the temperature range, perhaps including more replicas at low and high temperatures, without increasing the computational time. Extended sampling techniques like parallel tempering combined with the well-tempered ensemble are effective to capture more reliable properties. This is especially true when we want to compare the distribution of properties, instead of the average values. Further, several external conditions should be evaluated, such as temperature, ion concentrations, and solute concentrations, to characterize a given porin. Apart from reporting on the advantages of the enhanced sampling method in assessing the molecular properties of nanopores, our comparative analysis provided new and key results on structural/dynamical features correlated to the biological problem of the mass transport through nanopores. Eventually, PT-WTE simulations arrived at a level of precision to show a perfect match with key concepts developed using analytical treatments (binding, sat-

View Article Online
DOI: 10.1039/D3CP00935A

Table 2 Details of simulations performed during equilibration and production run (PrePT and PostPT MDs)

Simulation Time	T-coupling	Parameters	P-coupling	Parameters
200 ps 300K	Berendsen	1 ps, 3 groups	NO	NO
1ns 300K	Berendsen	1 ps, 3 groups	Berendsen	Semi-iso 5ps
30 ns 300K	V-rescale	1 ps, 3 groups	Parrinello-Rahman	Semi-iso 5 ps
300 ns 300K	V-rescale	1 ps, 3 groups	Parrinello-Rahman	Semi-iso 2 ps
10 ns 300K	V-rescale	1 ps, 1 group	NO	NO
1 μs 300K/350K	V-rescale	1 ps, 1 group	NO	NO
1 μs 300K/350K	V-rescale	1 ps, 1 group	NO	NO

Table 3 Parameters for Parallel Tempering simulations (PT) with 16 replicas (from 300ns/300K): T_{i+1}/T_i=1.01; T_{min}=297.03; T_{max}=344.842

Simulation Time	Method	Exchange time	Exchange rate	Ensemble
10 ns	Standard.	NO	NA	NVT
10 ns	Standard	200 fs	0.2 %	NVT
20 ns	Build META-WTE	NO	NA %	NVT
10 ns	META-WTE	200 fs	40 %	NVT
500 ns	META-WTE	200 fs	39 %	NVT
500 ns	META-WTE	200 fs	39 %	NVT

uration, kinetics), providing at the same time the molecular details. Thus they can be used to properly investigate the molecular properties of nanopores. This is particularly useful when designing beta-barrel pores for mass transport applications, where apart from a general mechanism that might be conserved, subtle amino acid substitutions can modulate key properties of transport.

4 Methods

4.1 Simulation protocols

We prepared OmpF/OmpC systems embedded in a pre-equilibrated POPC lipid bilayer, as done previously[47] from X-ray structures, respectively 2OMF and 2J1N. We protonated one residue behind the loop L3, as proposed in the past[56] and suggested by the software Propka (OmpF: Glu-296; OmpC: Asp-299). We solvated with water and added KCl ions to have a neutral system and a final concentration of 200 mM. We employed the Amber2014,[57] Gaff-Lipid[58] and Tip3p force fields;[59] simulations were performed with Gromacs[60], version 2020.2 run on the Marconi100 supercomputer at CINECA. We equilibrated the temperature and pressure for more than 300 ns as reported in Table 2. Then we performed 1 μs simulation at 300K and 345K in the NVT ensemble with standard MD (referred as PrePT MD). We also prepared and equilibrated 16 replicas in the same ensemble with temperatures ranging from 297K to 345K (the latter close to the maximum temperature of stability for such pores[51]), with a ratio between the temperature of neighbor replicas of 1.01.

Because of the high number of atoms (>100.000), the parallel tempering scheme (PT) cannot be applied over this large range of temperatures with only 16 replicas. From the test we performed, the exchange rate is less than 1%. The metadynamics well-tempered ensemble (WTE),[43] by increasing the fluctuations of the potential energy, permits to have a better overlap among replicas. In our case (see Table 3), after 20 ns for building the bias on the potential energy of replicas, we reached an exchange rate of 40%, which is acceptable. We then performed 1 μs simulations of PT in the WTE, obtaining a final exchange acceptance rate of 38%. After the PT simulations, we simulated for an additional 1 μs the replicas with T=300K and T=345K (referred as PostPT MD).

We calculated the size of internal pores using our in-house program.[61] For the PT simulations, the exchanges among replicas were performed every 100 steps, or 200 fs, in order to have maximum sampling efficiency.[62] The 16 replicas were simulated on 8 nodes, each with 4 GPU, thus assigning to each replica 2 GPU. This is the best arrangement on the Marconi100 hardware equipped with communications among pairs of GPUs. The performance obtained was 43/ns day.

4.2 Electrophysiology experiments

The single-channel electrophysiology experiments on porins reconstituted in lipid bilayer were performed by using a standard protocol we used previously[3,15,63]. To form a planar lipid bilayer with the lipid monolayer opposition technique[64], we used a 5 mg/mL solution of 1,2-diphytanoyl-sn-glycero-3-phosphocholine (Avanti Polar Lipids, Inc., Alabaster, AL) in pentane. A bilayer is formed across a 50–100 μm diameter aperture in a 25 μm thick Teflon partition. Silver chloride electrodes from WPI (World Precision Instruments), one connected to the live side of the amplifier (referred to as the trans side; where the voltage is applied) and the other connected to the ground side (referred to as the cis side), were used. A small amount (up to 0.1 μL) of wild-type OmpF from a diluted stock solution of 60 ng/mL in 1% (v/v) of genapol is added to the cis side of the chamber. Spontaneous insertion of a single OmpF channel usually happens within minutes after protein addition to the aqueous phase with a volume of 250 μL (1M KCl, 20 mM MES, pH 6). Both the small-ion conductance and the gating properties were used as an indication of directional channel insertion (likely with the cis side of the lipid bilayer corresponding to the extracellular side of the porin 80% of the time). Our convention is that the plus sign (positive voltage) means that the trans side of the membrane cell compartment is more positive. Conductance measurements were performed using an Axopatch 200B amplifier (Axon Instruments, Inc., Foster City, CA) in the voltage clamp mode. Data were filtered by a low-pass 4-pole Bessel filter at 10 kHz with a sampling frequency of 50 kHz or 250 kHz and recorded simultaneously into the computer

View Article Online
DOI: 10.1039/D3CP00935A

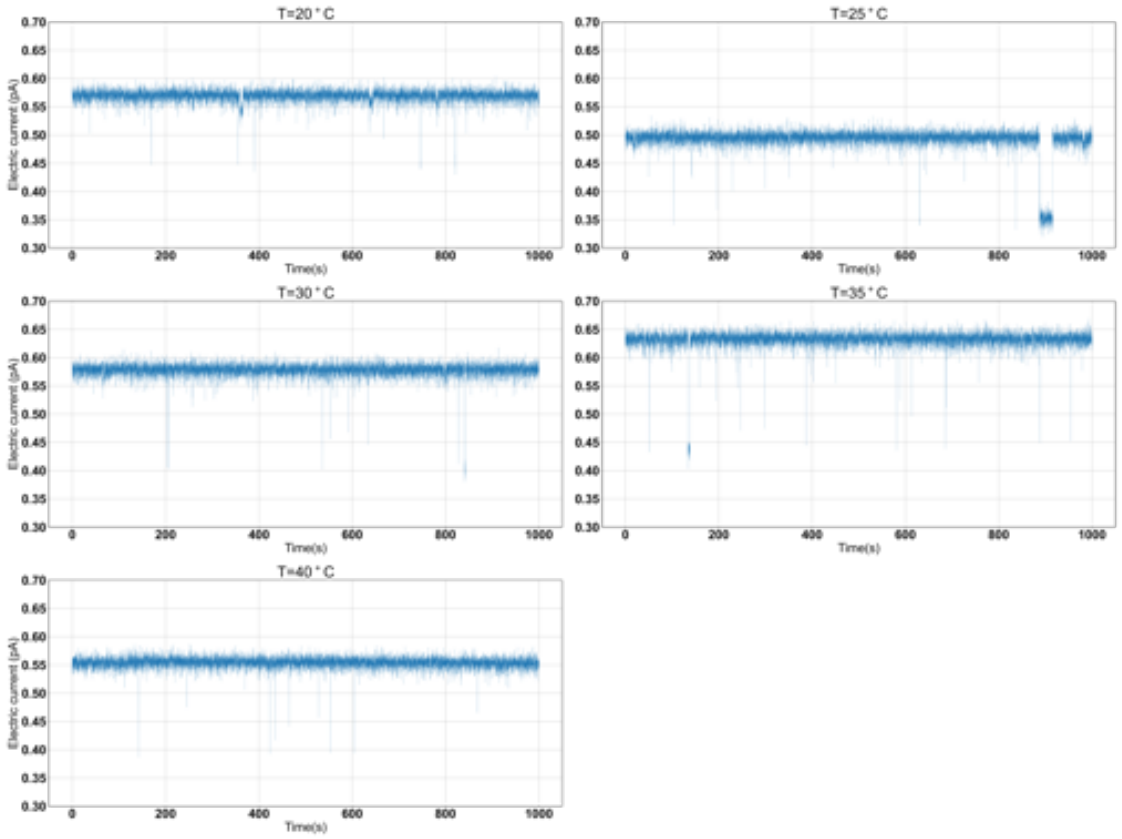

Fig. 9 Example of few current traces for 5 mM ertapenem through OmpF at different temperatures (pH 8, 1 M KCl and 100 mV)

memory.

Due to the heating of the amplifier, many times we observed an increase of temperature (up to 2–3 °C increase from room temperature) in the cuvette of small volumes (250 μL). For this reason the measurements were finished within 2–3 hours to minimize (although not completely eliminate; an increase to 1–1.5 °C is observed) conductance/transport properties fluctuation due to temperature changes. We performed several independent electrophysiology measurements varying the pH from 7 to 8, the electric field, from -100 mV to 100 mV, and the KCl ion concentration, 0.2 M and 1.0 M, as partially reported in Fig.9. The kinetics of all antibiotics to obtain Fig.8 (ETP=ertapenem; NFX=norfloxacin; CTX=cefotaxime; FEP=cefepime) were measured at 0.2M, pH 7, 1M KCl concentration and with an external applied electric field of -50 mV, but ertapenem, for which we used +50 mV. Concentrations of antibiotics used are: NFX=0.25mM; ETP=5mM; CTX=5mM; FEP=5mM. We analysed the event rates ($f_e = N_e/s^{-1}$) and mean dwell times τ_r, to assess the translocation of these molecules through these general diffusion porins, where τ_r is obtained from fitting an exponential to the distribution of dwell times, where N_e is the number of events in a given time interval.[65]

Author Contributions

SM, JW, and SG performed the investigation and formal analysis; MC supervised the work; MW and IB conceptualized the work. All authors contributed to writing, reviewing and editing the manuscript.

Conflicts of interest

There are no conflicts to declare.

Acknowledgements

The author thanks the ISCRA project PREDICT for providing CPU time on Marconi-100@Cineca. This research was partially supported by EU funding within the NextGeneration EU-MUR PNRR Extended Partnership initiative on Emerging Infectious Diseases (Project no. PE00000007, INF-ACT). IB was supported in part by the Agence Nationale de la Recherche (France), projet ANR BRIDGE AAP CE29. MW and IB acknowledge support from the JPIAMR network RESET-ME (Germany) (BMBF-ERANET JPIAMR - 01KI1827B).

Notes and references

1 R. Koebnik, K. P. Locher and P. V. Gelder, *Molecular microbiology*, 2000, **37**, 239 – 253.
2 M. S. Sansom, G. R. Smith, C. Adcock and P. C. Biggin, *Biophysical Journal*, 1997, **73**, 2404 – 2415.
3 H. Bajaj, S. Acosta-Gutierrez, I. Bodrenko, G. Malloci, M. A. Scorciapino, M. Winterhalter and M. Ceccarelli, *ACS nano*, 2017, **11**, 5465 – 5473.
4 A. Luscher, L. Moynié, P. S. Auguste, D. Bumann, L. Mazza, D. Pletzer, J. H. Naismith and T. Köhlera, *Antimicrobial agents*

View Article Online
DOI: 10.1039/D3CP00935A

and chemotherapy, 2018, **62**, 1062.

5 J. Vergalli, I. V. Bodrenko, M. Masi, L. Moynié, S. Acosta-Gutierrez, J. H. Naismith, A. Davin-Régli, M. Ceccarelli, B. v. d. Berg, M. Winterhalter and J.-M. Pagès, *Nature Reviews Microbiology*, 2020, **18**, 164 – 176.

6 R. Chowdhury, T. Ren, M. Shankla, K. Decker, M. Grisewood, J. Prabhakar, C. Baker, J. H. Golbeck, A. Aksimentiev, M. Kumar and C. D. Maranas, *Nature Communications*, 2018, **9**, 3661 – 10.

7 H. Bayley, *Clinical Chemistry*, 2015, **61**, 25 – 31.

8 U. Stein, A. Meller, Y. Rozevsky, T. Gilboa, X. F. V. Kooten, D. Kobelt and D. Huttner, *ACS nano*, 2020, **14**, 13964 – 13974.

9 H. Ouldali, K. Sarthak, T. Ensslen, F. Piguet, P. Manivet, J. Pelta, J. C. Behrends, A. Aksimentiev and A. Oukhaled, *Nature biotechnology*, 2020, 1 – 10.

10 N. S. Galenkamp, M. Soskine, J. Hermans, C. Wloka and G. Maglia, *Nature Communications*, 2018, **9**, 4085 – 8.

11 A. Siria, M.-L. Bocquet and L. Bocquet, *Nature Reviews Chemistry*, 2017, **1**, 0091.

12 A. A. Vorobieva, P. White, B. Liang, J. E. Horne, A. K. Bera, C. M. Chow, S. Gerben, S. Marx, A. Kang, A. Q. Stiving, S. R. Harvey, D. C. Marx, G. N. Khan, K. G. Fleming, V. H. Wysocki, D. J. Brockwell, L. K. Tamm, S. E. Radford and D. Baker, *Science*, 2021, **371**, year.

13 A. Mateus, J. Hevler, J. Bobonis, N. Kurzawa, M. Shah, K. Mitosch, C. V. Goemans, D. Helm, F. Stein, A. Typas and M. M. Savitski, *Nature Publishing Group*, 2020, 1 – 23.

14 S. K. R, K. Jana, A. H. Shaji, K. S. Nair, A. D. Das, D. Vikraman, H. Bajaj, U. Kleinekathöfer and K. R. Mahendran, *Nature Communications*, 2022, **13**, 5377.

15 I. V. Bodrenko, J. Wang, S. Salis, M. Winterhalter and M. Ceccarelli, *ACS Sensors*, 2017, **2**, 1184 – 1190.

16 H. Nikaido, *The Journal of antimicrobial chemotherapy*, 1988, **22 Suppl A**, 17 – 22.

17 T. F. Durand-Reville, A. A. Miller, J. P. O'Donnell, X. Wu, M. A. Sylvester, S. Guler, R. Iyer, A. B. Shapiro, N. M. Carter, C. Velez-Vega, S. H. Moussa, S. M. McLeod, A. Chen, A. M. Tanudra, J. Zhang, J. Comita-Prevoir, J. A. Romero, H. Huynh, A. D. Ferguson, P. S. Horanyi, S. J. Mayclin, H. S. Heine, G. L. Drusano, J. E. Cummings, R. A. Slayden and R. A. Tommasi, *Nature Publishing Group*, 2021, **597**, 698 – 702.

18 M. Winterhalter and M. Ceccarelli, *European journal of pharmaceutics and biopharmaceutics : official journal of Arbeitsgemeinschaft für Pharmazeutische Verfahrenstechnik eV*, 2015, **95**, 63 – 67.

19 R. Tommasi, R. Iyer and A. A. Miller, *ACS Infectious Diseases*, 2018, **4**, 686 – 695.

20 C. A. Lipinski, F. Lombardo, B. W. Dominy and P. J. Feeney, *Advanced drug delivery reviews*, 2001, **46**, 3 – 26.

21 D. Benkerrou and M. Ceccarelli, *Physical chemistry chemical physics : PCCP*, 2018, **20**, 8533 – 8546.

22 A. Pira, M. A. Scorciapino, I. V. Bodrenko, A. Bosin, S. Acosta-Gutierrez and M. Ceccarelli, *Molecules*, 2020, **25**, 5747.

23 M. F. Richter, B. S. Drown, A. P. Riley, A. Garcia, T. Shirai, R. L. Svec and P. J. Hergenrother, *Nature Publishing Group*, 2017, **545**, 299 – 304.

24 S. Acosta-Gutierrez, M. A. Scorciapino, I. Bodrenko and M. Ceccarelli, *Journal Of Physical Chemistry Letters*, 2015, **6**, 1807 – 1812.

25 A. Laio and M. Parrinello, *Proceedings of the National Academy of Sciences of the United States of America*, 2002, **99**, 12562 – 12566.

26 S. Acosta-Gutierrez, I. V. Bodrenko and M. Ceccarelli, *Antibiotics (Basel, Switzerland)*, 2021, **10**, 635.

27 D. Jeanteur, T. Schirmer, D. Fourel, V. Simonet, G. Rummel, C. Widmer, J. P. Rosenbusch, F. Pattus and J. M. Pagès, *Proceedings of the National Academy of Sciences*, 1994, **91**, 10675–10679.

28 H. Lou, M. Chen, S. S. Black, S. R. Bushell, M. Ceccarelli, T. Mach, K. Beis, A. S. Low, V. A. Bamford, I. R. Booth, H. Bayley and J. H. Naismith, *PLoS ONE*, 2011, **6**, e25825.

29 L. Pulzova, L. Navratilova and L. Comor, *Microbial Drug Resistance*, 2017, **23**, 413–420.

30 S. David, J. L. C. Wong, J. Sanchez-Garrido, H.-S. Kwong, W. W. Low, F. Morecchiato, T. Giani, G. M. Rossolini, S. J. Brett, A. Clements, K. Beis, D. M. Aanensen and G. Frankel, *PLoS Pathogens*, 2022, **18**, e1010334.

31 I. V. Bodrenko, S. Salis, S. Acosta-Gutierrez and M. Ceccarelli, *Journal Of Chemical Physics*, 2019, **150**, 211102.

32 M. A. Scorciapino, S. Acosta-Gutierrez, D. Benkerrou, T. D'Agostino, G. Malloci, S. Samanta, I. Bodrenko and M. Ceccarelli, *Journal of physics. Condensed matter : an Institute of Physics journal*, 2017, **29**, 113001.

33 S. Acosta-Gutierrez, L. Ferrara, M. Pathania, M. Masi, J. Wang, I. Bodrenko, M. Zahn, M. Winterhalter, R. A. Stavenger, J.-M. Pagès, J. H. Naismith, B. v. d. Berg, M. G. P. Page and M. Ceccarelli, *ACS Infectious Diseases*, 2018, **4**, 1487 – 1498.

34 S. Acosta-Gutierrez, I. Bodrenko, M. A. Scorciapino and M. Ceccarelli, *Physical chemistry chemical physics : PCCP*, 2016, **18**, 8855 – 8864.

35 B. v. d. Berg, S. P. Bhamidimarri, J. D. Prajapati, U. Kleinekathöfer and M. Winterhalter, *Proceedings of the National Academy of Sciences*, 2015, **112**, E2991 – 9.

36 M. Invernizzi and M. Parrinello, *J. Phys. Chem. Lett.*, 2020, **11**, 1 – 6.

37 D. Winogradoff, H.-Y. Chou, C. Maffeo and A. Aksimentiev, *Nature Communications*, 2022, 1 – 16.

38 S. Piana, K. Sarkar, K. Lindorff-Larsen, M. Guo, M. Gruebele and D. E. Shaw, *Journal of molecular biology*, 2011, **405**, 43 – 48.

39 K. Lindorff-Larsen, S. Piana, R. O. Dror and D. E. Shaw, *Science*, 2011, **334**, 517 – 520.

40 O. Valsson, P. Tiwary and M. Parrinello, *Annual Review of Physical Chemistry*, Annual Review of Physical Chemistry, 2016, vol. 67, pp. 159 – 184.

41 P. Tiwary, V. Limongelli, M. Salvalaglio and M. Parrinello, *Proceedings of the National Academy of Sciences*, 2015, **112**, E386

View Article Online
DOI: 10.1039/D3CP00935A

– 91.

42 A. T. Weigle, M. Carr and D. Shukla, *Journal of Chemical Theory and Computation*, 2021, **17**, 5342–5357.

43 M. Bonomi and M. Parrinello, *Physical review letters*, 2010, **104**, 190601.

44 V. Shoshan-Barmatz, V. D. Pinto, M. Zweckstetter, Z. Raviv, N. Keinan and N. Arbel, *Molecular aspects of medicine*, 2010, **31**, 227 – 285.

45 S. Biswas, M. M. Mohammad, D. R. Patel, L. Movileanu and B. v. d. Berg, *Nature Structural and Molecular Biology*, 2007, **14**, 1108 – 1109.

46 M. Zahn, S. P. Bhamidimarri, A. Baslé, M. Winterhalter and B. v. d. Berg, *Structure*, 2016, **24**, 221 – 231.

47 A. Kumar, E. Hajjar, P. Ruggerone and M. Ceccarelli, *Journal Of Physical Chemistry B*, 2010, **114**, 9608 – 9616.

48 D. Zhang, Y. M. Yip and L. Li, *Mitochondrion*, 2016, **30**, 222–228.

49 D. Vikraman, R. Satheesan, M. Rajendran, N. A. Kumar, J. B. Johnson, S. K. R and K. R. Mahendran, *ACS Sensors*, 2022, **7**, 1766–1776.

50 A. K. Vasan, N. Haloi, R. J. Ulrich, M. E. Metcalf, P.-C. Wen, W. W. Metcalf, P. J. Hergenrother, D. Shukla and E. Tajkhorshid, *Proceedings of the National Academy of Sciences*, 2022, **119**, 2117009119.

51 I. Biró, S. Pezeshki, H. Weingart, M. Winterhalter and U. Kleinekathöfer, *Biophysical Journal*, 2010, **98**, 1830 – 1839.

52 I. Galdadas, S. Lovera, G. Pérez-Hernández, M. D. Barnes, J. Healy, H. Afsharikho, N. Woodford, R. A. Bonomo, F. L. Gervasio and S. Haider, *Scientific Reports*, 2018, **8**, 1135.

53 I. V. Bodrenko, S. Milenkovic and M. Ceccarelli, *Biomolecular concepts*, 2022, **13**, 207 – 219.

54 B. K. Ziervogel and B. Roux, *Structure/Folding and Design*, 2012, 1 – 12.

55 M. Jensen, S. Park, E. Tajkhorshid and K. Schulten, *Proceedings of the National Academy of Sciences of the United States of America*, 2002, **99**, 6731 – 6736.

56 S. Varma, S.-W. Chiu and E. Jakobsson, *Biophysical Journal*, 2006, **90**, 112 – 123.

57 K. Lindorff-Larsen, S. Piana, K. Palmo, P. Maragakis, J. L. Klepeis, R. O. Dror and D. E. Shaw, *Proteins*, 2010, **78**, 1950 – 1958.

58 C. J. Dickson, L. Rosso, R. M. Betz, R. C. Walker and I. R. Gould, *Soft Matter*, 2012, **8**, 9617.

59 W. L. Jorgensen, J. Chandrasekhar, J. D. Madura, R. W. Impey and M. L. Klein, *Journal Of Chemical Physics*, 1983, **79**, 926.

60 M. J. Abraham, T. Murtola, R. Schulz, S. Páll, J. C. Smith, B. Hess and E. Lindah, *SoftwareX*, 2015, **1-2**, 19 – 25.

61 A. Kumar, E. Hajjar, P. Ruggerone and M. Ceccarelli, *Journal of Physics: Condensed Matter*, 2010, **22**, 454125.

62 D. J. Sindhikara, D. J. Emerson and A. E. Roitberg, *Journal Of Chemical Theory And Computation*, 2010, **6**, 2804 – 2808.

63 K. R. Mahendran, C. Chimerel, T. Mach and M. Winterhalter, *European biophysics journal : EBJ*, 2009, **38**, 1141 – 1145.

64 M. Montal and P. Mueller, *Proceedings of the National Academy of Sciences*, 1972, **69**, 3561 – 3566.

65 L. Kullman, M. Winterhalter and S. M. Bezrukov, *Biophysical Journal*, 2002, **82**, 803 – 812.